

Constructing unsaturated coordination Co–M (M = P, S, Se, Te) bonds modified metallic Co for efficient alkaline hydrogen evolution

Zehao Zang^a, Yangyang Ren^a, Chunyan Fan^a, Yahui Cheng^b, Lanlan Li^a, Xiaofei Yu^a, XIAOJING YANG^a, Zunming Lu^a, Xinghua Zhang^{a,*}, Hui Liu^{c,*}

^a School of Materials Science and Engineering, Hebei University of Technology, Tianjin 300130, China

^b Tianjin Key Laboratory of Process Control and Green Technology for Pharmaceutical Industry, Department of Electronics, Nankai University, Tianjin 300350, China

^c School of Materials Science and Engineering, Tianjin University, Tianjin 300072, China



ARTICLE INFO

Keywords:

Hydrogen evolution reaction
Metallic Co
Unsaturated coordination
Local electronic structure
Density functional theory

ABSTRACT

Alkaline hydrogen evolution reaction (HER) provides a promising approach for producing green hydrogen, but designing high-efficiency transition metal nanocatalysts is rather challenging. Herein, unsaturated coordination Co–M (M = P, S, Se, Te) bonds modified metallic Co are designed on Ni foam (M-Co/NF) through a facile electrodeposition strategy. The constructed Co–M bonds not only alter the local coordination condition and electron structure, but also provide an electron transfer channel, and significantly enhance the intrinsic activities. Consequently, the P-Co/NF displays an ultralow overpotential of 23 mV at 10 mA cm⁻² with excellent stability. X-ray absorption spectroscopy verifies the formation of extremely unsaturated coordination Co–P bonds, which adjusts the charge redistribution. Density functional theory calculations prove the unsaturated coordination Co–P bonds can optimize the adsorption of H₂O and H adsorption. This work provides novel insight into the effects of local coordination environment on activity and the rational design of efficient transition metal nanocatalysts.

1. Introduction

Renewable energy-powered electrolysis of water into green hydrogen provides an important path to carbon neutrality [1–3]. Hydrogen evolution reaction (HER) is the core reaction to produce H₂ through electrochemical water splitting. However, HER process, especially in alkaline system, suffers from sluggish kinetics and heavy energy consumption, therefore, effective and low-cost electrocatalysts are imperative to drive alkaline HER [4,5]. To date, electrocatalysts based on precious metal materials are the most efficient catalysts which display lower overpotentials, such as Pt/C and Ru, while their inherent features limit the widespread applications [6,7]. Non-noble transition metals are deemed to be the ideal alternative catalysts for precious metal materials. However, most transition metals exhibit either too strong or too weak H binding ability, showing much lower performance than the precious metal catalysts [8,9]. In addition, the adsorption and dissociation process of H₂O molecules extremely affects the kinetics in alkaline electrolyte [10–12]. Therefore, optimizing HER behavior of non-noble transition metals to obtain superior activity to Pt/C is meaningful but

challenging.

Among non-noble transition metals, nickel and cobalt display relatively high HER performance and have attracted much attention. Compared with nickel (14.3×10^6 S m⁻¹), cobalt (Co) exhibits a higher conductivity of 15.7×10^6 S m⁻¹, which is more conducive to electron transport. In addition, the features of metallic Co, such as abundant reserves, moderate price and adjustable subshell structure, endow it with wide application in catalysis [13,14]. However, metallic Co exhibits inferior HER performance at moderate current density since the excessive Co–H bonding energy and insufficient adsorption and activation of H₂O molecules [15,16]. In addition, the insufficient adsorption and activation of H₂O can not provide enough available protons to produce hydrogen in alkaline environment, and the excessive adsorption of H intermediate makes it difficult to desorb H₂ [17,18]. Consequently, strategies for designing efficient metallic Co catalysts with enhanced adsorption and activation of H₂O and weakened H bonding are urgently developed.

Transition metal-based compounds, such as phosphates and sulfides, exhibit good HER activity due to their rich and adjustable chemical

* Corresponding authors.

E-mail addresses: zhangxinghua@hebut.edu.cn (X. Zhang), hui_liu@tju.edu.cn (H. Liu).

composition [19]. Moreover, the high-valence metal sites in the compounds have a stronger covalency of the M–O interaction and electrophilicity, which promote the adsorption of water molecules [20,21]. However, transition metal-based compounds exhibit poor electrical conductivity, and the high-valence metal substances will be reduced to low-valence metals at the reduction potential, which seriously affects the durability of the catalysts under working conditions, especially at large current density [22–24]. Qiao's group found that unsaturated compounds on metal surfaces and unsaturated chemical bonds in compounds are active for catalytic reactions [25,26]. Generally speaking, the metallic active center with low valence is considered to be the active site of metal phase catalysts for reductive HER [27]. Recent research has found that positively charged surface of transition metals as well as noble metals exhibit more suitable H adsorption strength [28–30]. Therefore, it is of great significance to seek the balance between transition metals and compounds to design HER catalysts with high activity and stability under high current density. Inspired by the above thoughts, introducing non-metallic elements into metallic Co to form Co–M (M: non-metallic elements) coordination bonds to serve as electron transfer channels may be an effective strategy to regulate surface charge states and optimize the catalytic activity. However, due to the easy formation of corresponding compounds, it is difficult to realize transition metal catalysts modified by non-metallic chemical bonds [31]. Moreover, the introduction of non-metallic elements usually requires a redundant synthesis process, accompanied by programmed temperature control and the release of harmful gases such as NH₃, H₂S or PH₃ [32,33]. How to achieve transition metal catalysts modified by non-metallic chemical bonds in a simple, gentle and scalable pathway is of great significance.

Herein, we report a facile and scalable electrodeposition strategy to prepare unsaturated coordination Co–M bonds modified metallic Co catalysts on Ni foam (M-Co/NF, M=P, S, Se, Te) for alkaline HER. The formation of unsaturated coordination Co–M bonds provides a channel of electron transfer, thus adjusting the local charge distribution and surface charge states. Therefore, the representative P-Co/NF catalyst exhibits distinguished performance, and only needs 23 and 85 mV to attain 10 and 100 mA cm⁻², which surpasses the commercial Pt/C. Theoretical calculations confirm that the unsaturated coordination Co–P bonds induce electron transfer from Co atoms to P atoms, enhance the H₂O adsorption, and weaken the binding energy of H. Besides, the incorporated P atoms facilitate the activation of H₂O via attracting protons in H₂O, and act as additional H adsorption sites. This work provides the rational design of high-efficiency non-noble transition metal catalysts and novel insight to the surface valence bond–activity relationship.

2. Experimental section

2.1. Materials

2.1.1. Preparation of the P-Co/NF

The P-Co/NF catalysts were obtained through an electrodeposition process in a two-electrode system on a constant voltage source at room temperature, in which nickel foam (NF, 2 cm × 3 cm) and carbon paper (CP, 2 cm × 3 cm) were used as cathode and anode, respectively. Before electrodeposition, NF was washed with 3.0 M HCl, deionized water and ethanol, and CP was also washed with deionized water and ethanol. The electrodeposition process was carried out in 50 mL electrolyte containing 50 mM CoCl₂·6H₂O, 1.25 M NH₄F and 125 mM NaH₂PO₂·H₂O. The electrodeposition voltage is 3.5 V and the electrodeposition time is 30 min. After washing the sample with deionized water and ethanol, the P-Co/NF was obtained. The loading of P-Co/NF catalyst is 18.8 mg cm⁻². In addition, the effects of deposition voltages, time and NaH₂PO₂·H₂O concentration on HER performance of P-Co/NF catalysts were explored.

2.1.2. Preparation of the Co/NF

The preparation process of Co/NF is similar to that of P-Co/NF, except that NaH₂PO₂·H₂O is not added to the electrolyte, and the loading of Co/NF catalyst is 13.3 mg cm⁻².

2.1.3. Preparation of the Co₂P/NF

Co₂P/NF contrast sample was prepared by a two-step process. First, Co/NF was prepared by electrodeposition, and then the Co/NF sample was treated by low-temperature phosphating. Specifically, a porcelain boat with prepared Co/NF was placed downstream of the tube furnace, and another porcelain boat with 1 g NaH₂PO₂·H₂O was placed upstream of the tube furnace, and then heated to 500 °C under N₂ atmosphere at a rate of 5 °C min⁻¹. After maintaining for 2 h, it was cooled naturally to room temperature, and the Co₂P/NF was obtained. The loading of Co₂P/NF is 19.4 mg cm⁻².

2.1.4. Preparation of the Pt/C/NF

The Pt/C electrode ink which contains 5 mg 20 % Pt/C, 720 μL deionized water, 250 μL isopropanol and 30 μL Nafion were ultrasonic treated for 30 min and then 50 μL ink was dropped on NF (1 cm × 1 cm) to serve as Pt/C/NF electrode.

2.1.5. Preparation of the M-Co/NF

The preparation conditions of S-Co/NF, Se-Co/NF and Te-Co/NF were similar to the P-Co/NF, except that the types of non-metallic sources are different in concentration. The S-Co/NF was prepared at 1 M CS(NH₂)₂ and its loading is 16.4 mg cm⁻². Se-Co/NF was prepared at 10 mM SeO₂ and its loading is 2.6 mg cm⁻². Te-Co/NF was prepared at 5 mM Na₂TeO₃ and its loading is 3.1 mg cm⁻².

2.2. Materials characterizations, Electrochemical and Computational Methods

The materials characterizations, electrochemical and computational methods are described in [supporting information](#) in detail.

3. Results and discussion

3.1. Physicochemical characterization

The metallic P-Co/NF catalyst with unsaturated Co–P coordination bonding was prepared via a facile and ingenious one-step electrodeposition method and the synthesis process is shown in [Fig. 1a](#). When applying a high potential of 3.5 V, the Co²⁺ and H₂PO₂⁻ ions migrate rapidly towards cathode and anode, respectively. The metallic Co was deposited on the surface of NF via the electroreduction of Co²⁺ at the cathode. Due to the large number of the H₂PO₂⁻ ions migrating to the anode driven by the potential, the concentration of H₂PO₂⁻ ions near the cathode is rapidly reduced, thus inhibiting the formation of cobalt phosphide. More importantly, the residual H₂PO₂⁻ ions near the cathode were adsorbed on the electron surface and reduced to P atoms which were incorporated into the lattice of metallic Co to form unsaturated coordination bonds. The reaction equations are as follows[34]:



To investigate the effect of unsaturated coordination Co–P bonding on HER performance, the pure Co/NF and Co₂P/NF catalysts were also prepared through electrodeposition and low-temperature phosphating, respectively. [Fig. 1b](#) displays the powder XRD patterns of different ultrasonic exfoliated powder samples. The pure Co sample shows three distinct diffraction peaks at 41.7°, 44.8° and 47.6°, which match with the (100), (001) and (101) planes of hexagonal phase metallic Co (PDF#05–0727), respectively. After introducing P element, due to the incorporated P atoms influencing the long-range ordering and local

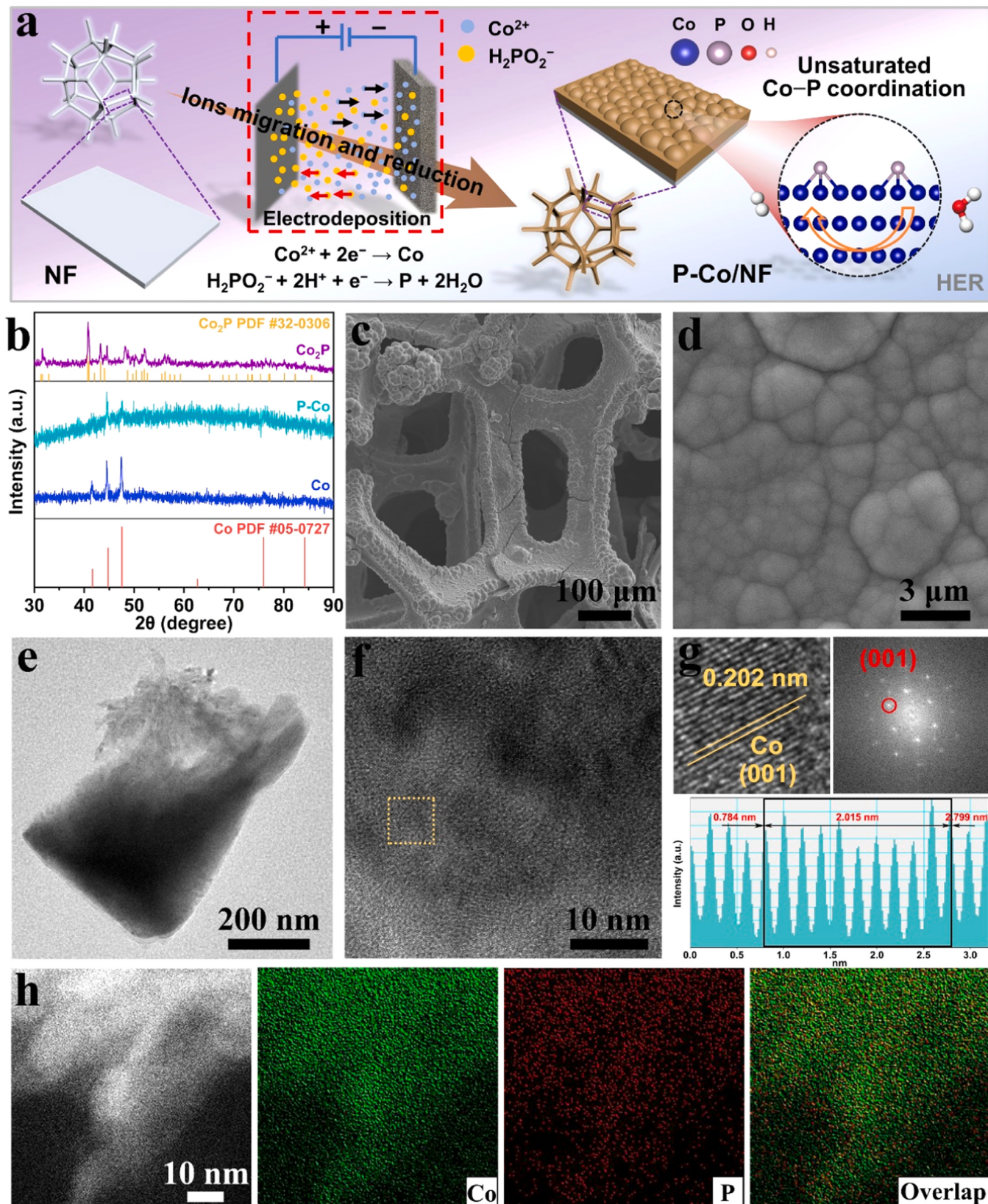


Fig. 1. (a) Schematic diagram of the synthesis of P-Co/NF, (b) XRD patterns of Co, P-Co and Co₂P, SEM image of P-Co/NF at (c) low and (d) high magnification, (e) TEM image, (f) HRTEM and (g) FFT pattern of P-Co, (h) AC-HAADF-STEM image and element mapping of P-Co catalyst.

coordination condition, only (001) and (101) planes were detected in P-Co, and the peak intensity is also reduced. Additionally, other diffraction peaks were not detected in P-Co catalyst, indicating that the introduced P atoms did not alter the host structure and no detectable compounds were formed. After low-temperature phosphating of Co/NF, typical diffraction peaks of Co_2P (PDF#32-0306) appear, indicating that the phase of Co/NF is transformed into Co_2P . The micro-morphology of P-Co/NF was characterized through scan electron microscopy (SEM). As shown in Fig. 1c, a dense catalyst layer of P-Co can be clearly observed, and in the

magnified SEM image, the surface of P-Co/NF exhibits a smooth membrane structure, where prominent smooth particles can be observed, and the interface of the stacked particles can also be seen on the surface of the membrane structure, indicating that the P-Co/NF is a film-like structure assembled by particles with smooth surface (Fig. 1d). In addition, the atomic content of P in P-Co/NF is 13.5 %, indicating the successful introduction of P atoms in P-Co sample (Table S1). The microstructure of P-Co was further analyzed by transmission electron microscopy (TEM) and aberration-corrected TEM (AC-TEM). The TEM image of P-Co displays a blocky structure (Fig. 1e), matching well with SEM results. Moreover, the high-resolution TEM (HRTEM) image displays shorter staggered oriented lattice stripes, indicating the poor crystallinity of P-Co (Fig. 1f). The lower crystallinity is conducive to exposing more unsaturated coordination Co atoms, thereby facilitating

the catalytic reaction [35,36]. In addition, the interplanar spacing is 0.202 nm, corresponding to the (001) plane of Co, and this plane is also found in the fast Fourier transform image (FFT), further proving the metallic phase of P-Co (Fig. 1g). Moreover, the elements distribution of P-Co in the microregion was analyzed through AC-HAADF-STEM. As shown in Fig. 1h, Co and P elements display uniform distribution in the microregion of P-Co, implying the P element is successfully introduced into the P-Co catalyst.

Different from the membrane structure of P-Co/NF, the pure metallic Co/NF grows vertically on the NF skeleton in the form of an interleaved array of nanosheets (Fig. S1). TEM images further confirm the nanosheet morphology of pure Co (Fig. S2a). The lattice fringes of pure Co have a relatively consistent trend with the interplanar spacing of 0.202 nm, indicating that the formed pure Co nanosheets have good crystallinity (Fig. S2b). After phosphating, the microstructure of the $\text{Co}_2\text{P}/\text{NF}$ changes from the nanosheet structure to the particles (Fig. S3 and S4a), and the lattice fringe of 0.221 nm is assigned to the (121) plane of Co_2P (Fig. S4b).

The chemical valence bond and electronic configuration of different catalysts were investigated through X-ray photoelectron spectroscopy (XPS). Co 2p spectrum of P-Co displays Co^0 (777.65 eV and 792.70 eV), Co^{3+} (780.61 eV and 796.41 eV), Co^{2+} (781.83 eV and 797.11 eV) and a pair of satellite peaks (Fig. 2a) [37–39]. The appearance of Co^{2+} and Co^{3+} is due to unavoidable natural oxidation [40]. Compared with pure

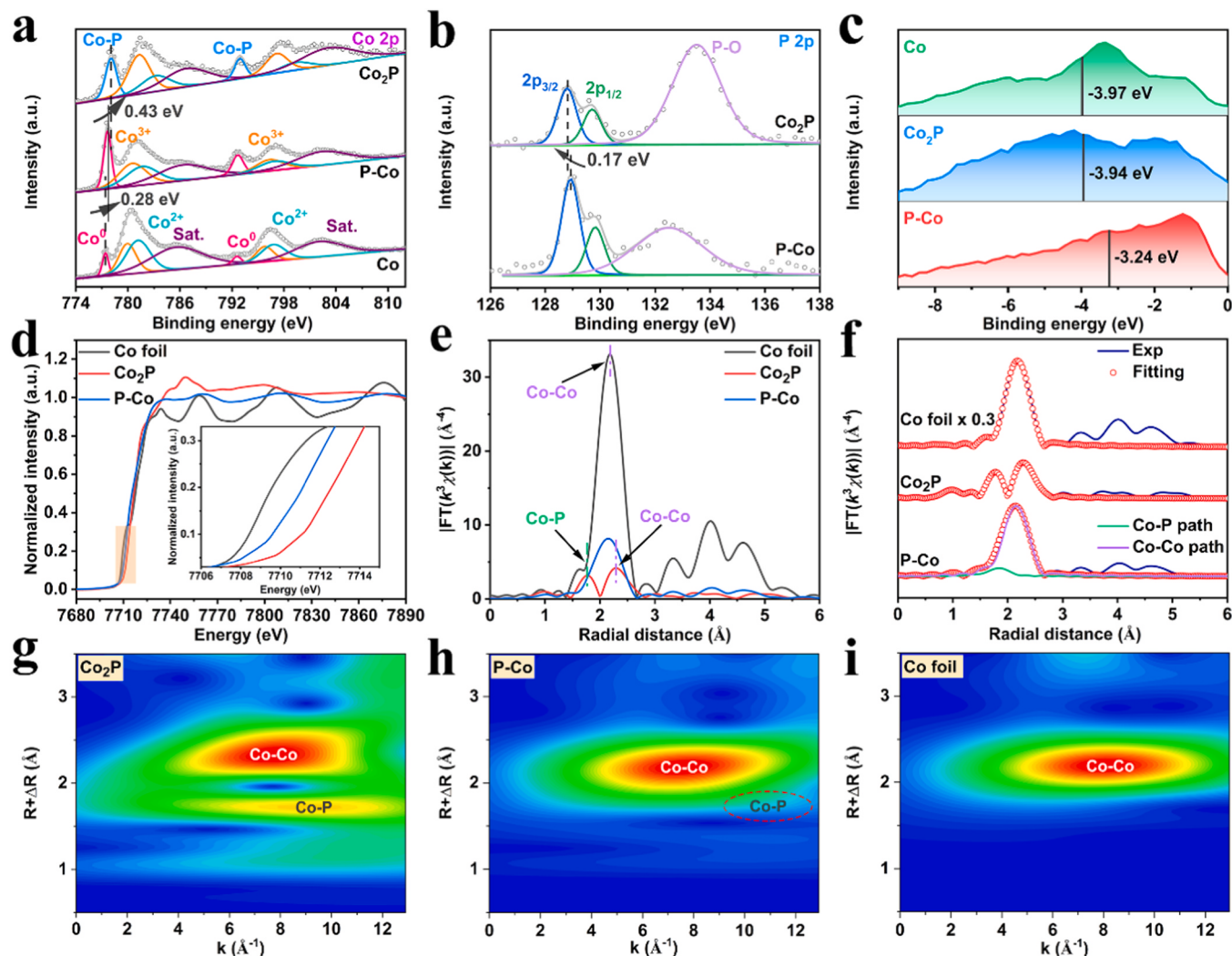


Fig. 2. (a) Co 2p, (b) P 2p and (c) normalized valence band spectra of Co_2P , P-Co and Co. (d) Co K-edge XANES and (e) FT-EXAFS spectra of Co foil, Co_2P and P-Co and (f) their fitting results in R-space. Wavelet transforms for the k^3 -weighted Co K-edge EXAFS signals of (g) Co_2P , (h) P-Co and (i) Co foil.

Co, the binding energy of Co⁰ peak in P-Co shifts 0.28 eV towards higher binding energy, but lower than the binding energy of Co–P bond in Co₂P, which indicates that the valence state of Co atom in P-Co is between pure Co and Co₂P[41]. In addition, the Co⁰ content in Co/NF is lower than that in P-Co/NF. This is related to the degree of surface oxidation of the samples. P-Co/NF displays a smooth membrane structure (Fig. 1d), while Co/NF shows a vertically staggered nanosheet structure (Fig. S1), which leads to more serious surface oxidation, and decreases the content of Co⁰ in Co/NF. For the P 2p spectrum of P-Co, the peak of 128.90 eV corresponds to the Co–P bond and the wide peak of 132.40 eV is attributed to the phosphorus oxide (Fig. 2b) [42,43]. While the binding energy of Co₂P is negatively shifted by 0.17 eV, manifesting the electron density of P in P-Co is lower than that of Co₂P. All these results suggest that the introduced P atoms regulate the electronic structure of P-Co through the Co–P bonds. Additionally, the valence band spectra of different catalysts were tested through XPS and the d-band centers were calculated. The d-band center value of P-Co is –3.24 eV, which is higher than that of pure Co (–3.97 eV) and Co₂P (–3.94 eV) (Fig. 2c). The introduction of P atoms induces the upshift of d-band center for P-Co which is closer to Fermi level, indicating that the P-Co catalyst has stronger affinity for H₂O molecules, thus promoting the HER activity [44,45].

X-ray absorption fine structure (XAFS) was adopted to further analyze the effects of the P atoms on the local coordination environment and valence bond structure of P-Co catalyst. Fig. 2d shows the Co K-edge X-ray absorption near edge structure (XANES) spectra. The XANES spectrum of P-Co is similar to the Co foil, but significantly different from Co₂P, indicating the metallic phase of P-Co. In addition, the absorption edge of P-Co is located between Co foil and Co₂P, and the absorption edge of P-Co displays significantly positive shift compared with Co foil, indicating that the electrons transfer from Co atoms to P atoms through Co–P bonds, which is consistent well with the XPS results. Moreover, the local geometric coordination condition of Co atoms in P-Co is analyzed by Fourier-transformed extended X-ray adsorption fine structure (EXAFS) spectra, and the dominant peak in Co foil is located at 2.18 Å, which is assigned to Co–Co scattering. For the EXAFS spectrum of Co₂P, two main coordination peaks appear around 1.76 Å and 2.29 Å, which are attributed to Co–P and Co–Co scattering[42,46], respectively. For the spectrum of P-Co, the main coordination peak of the Co–Co bond is around 2.14 Å which is between the Co–Co bond of Co foil and the Co–P bond of Co₂P, indicating that the introduction of P makes the average bond length of Co–Co bond slightly decrease (Fig. 2e). The coordination conditions of chemical bonds in P-Co are further elucidated through the fitting of EXAFS. Fig. 2f and Table S2 show the fitting spectra and fitting results of Co foil, Co₂P and P-Co catalysts. The coordination number of Co–Co bond in P-Co is 3.8, which is much lower than that of Co foil. In addition, the Co–P coordinate bond in P-Co is confirmed through fitting the P-Co coordination peak, and the Co–P coordination number is 0.4, which is much lower than the Co–P coordination number of Co₂P (4.9), indicating the existence of highly unsaturated Co–P bonds in P-Co catalyst.

Fig. S5 displays the oscillation curves of Co foil, Co₂P and P-Co in K space and their fitting results. The oscillation function of P-Co is similar to the Co foil, but significantly different from Co₂P, further confirming the metallic phase of P-Co. In addition, compared with Co foil, the amplitude of P-Co is markedly reduced, implying the local atomic arrangement of P-Co is slightly different from Co foil. The oscillations of EXAFS are further analyzed by wavelet transform (WT). For the WT of Co₂P, the maximum intensity appears at 7.7 Å^{–1} and 9.3 Å^{–1} (Fig. 2g), corresponding to the oscillating signals of the Co–Co and Co–P coordination bonds, respectively. The maximum intensity of Co foil appears at 8.3 Å^{–1}, which corresponds to the oscillation signal of the Co–Co bonds in the metal phase (Fig. 2i). However, the maximum intensity of P-Co negatively shifts to 7.6 Å^{–1}, which is related to the unsaturated Co–P bond changing the local coordination environment. Moreover, the oscillating signal of Co–P coordination bond appears at 10–12 Å^{–1},

which further confirms the existence of the Co–P coordination bonds in P-Co catalyst (Fig. 2h). In addition, the WT vibration function of P-Co is similar to the Co foil, but significantly different from Co₂P, indicating there is no formation of bulk cobalt phosphide in P-Co. Based on XPS and XAFS results, the incorporated P atoms bind with Co atoms to form unsaturated Co–P coordination bonds, inducing electrons transfer from Co atoms to P atoms via the Co–P channel, essentially regulating the local coordination environment and electronic structure of P-Co, thereby facilitating the improvement of electrocatalytic performance.

More importantly, this electrodeposition strategy can also be used to construct other unsaturated coordination chemical bonds on the metallic Co such as S-Co/NF, Se-Co/NF and Te-Co/NF. The XRD patterns indicate that S-Co/NF, Se-Co/NF and Te-Co/NF are all metallic Co phase (Fig. S6a). SEM and TEM results confirm that the morphology of S-Co/NF, Se-Co/NF and Te-Co/NF is the random stacking structure of nanoparticles, and the non-metallic elements and Co element are uniformly distributed on the catalyst surface (Fig. S7 and S8). Similar to the XPS spectra of P-Co, the XPS spectra of M-Co (M = S, Se, Te) shift 0.30 or 0.20 eV towards high binding energy, and the M²⁺ peaks appear in the XPS spectra of M elements, indicating the formation of Co–M bonds in M-Co catalysts (Fig. S6b and S6c).

3.2. HER activities of M-Co/NF

The HER performance of M-Co/NF was evaluated with a typical three-electrode system in 1.0 M KOH. To investigate the effect of preparation process on catalyst performance, a series of M-Co/NF catalysts were prepared under different conditions. For the P-Co/NF catalyst, the effects of deposition potential, time and NaH₂PO₂ concentration on HER performance were investigated. As shown in Fig. S9–11, with the increase of deposition potential, time and NaH₂PO₂ concentration, the overpotential of the sample at 10 mA cm^{–2} first decreases and then increases. When the deposition potential is 3.5 V, the deposition time is 30 min, and the concentration of NaH₂PO₂ is 125 mM, the sample has the best HER activity.

To confirm the origin of the superior performance of the P-Co/NF, the XRD patterns of a series of P-Co/NF catalysts with different deposition potentials and NaH₂PO₂ concentrations were tested, and the XRD peaks of different samples were carefully examined. As shown in Fig. S12, all the samples exhibit typical metallic Co diffraction peaks, and the locally amplified XRD patterns display no obvious deviation of the diffraction peaks, indicating that there was no lattice distortion in the catalysts. To investigate the relationship between the preparation conditions of the P-Co/NF catalysts and the catalytic performance. The loading, morphology and element contents of different catalysts were analyzed. With the increase of deposition potentials and deposition times, the loading of catalyst increases gradually, while the change of NaH₂PO₂ concentrations has no obvious effect on the loading of the catalysts (Table S3). Generally speaking, the increase of loading is conducive to increasing the number of active sites, but excessive loading can affect the charge and mass transport. Therefore, a moderate loading is beneficial for improving the catalytic performance. The SEM images of P-Co/NF catalysts prepared with different potentials are shown in Fig. S13. As the deposition potential increases, the morphology of the catalysts changes from small particles to a smooth membrane composed of particles, and finally to an irregularly stacked morphology of particles. It can also be observed from low magnification SEM images that the loading gradually increases with increasing potential. According to the SEM-EDS results (Table S4), the content of P increases gradually with the increase of deposition potential. When changing the deposition time, the catalysts display membrane structure. With the increase of deposition time, the particles composing the membrane gradually become larger and their surface becomes smoother (Fig. S14). In addition, the content of P element does not change significantly (Table S5). With the increase of NaH₂PO₂ concentrations, the size of the particles composing the membrane is increased (Fig. S15). More importantly, the content of P

element in the sample gradually increases (Table S6). Based on the above results, the excellent HER performance of P-Co/NF prepared with 125 mM Na₂HPO₄ at 3.5 V depositing 30 min is related to its moderate loading and P element content.

Based on the deposition potential and time of P-Co/NF, the effects of CS(NH₂)₂, SeO₂ and Na₂TeO₃ concentrations on the performance of S-Co/NF, Se-Co/NF and Te-Co/NF have also been investigated. For the S-Co/NF and Te-Co/NF, with the increase of the CS(NH₂)₂ and Na₂TeO₃ concentrations, the overpotential of the samples at 10 mA cm⁻² first decreases and then increases (Fig. S16 and S18). When the concentration of CS(NH₂)₂ is 1.0 M, and the concentration of Na₂TeO₃ is 5 mM, the S-Co/NF and Te-Co/NF have the best HER activity. For the Se-Co/NF, with the increase of the SeO₂ concentration, the overpotential of the samples at 10 mA cm⁻² gradually decreases (Fig. S17). Unfortunately, XRD patterns of Se-Co/NF prepared with different SeO₂ concentrations suggest that the catalyst prepared with low concentration SeO₂ is metallic Co phase (Fig. S19a). With the increase of SeO₂ concentration, the phase of the catalyst gradually changes into a mixed phase of metallic Co and Co_{0.85}Se. When the SeO₂ concentration is 70 mM, the prepared catalyst is pure Co_{0.85}Se (Fig. S19b). Therefore, the Se-Co/NF prepared with 10 mM SeO₂ possesses good performance as Se-Co/NF catalyst. Similar to the Se-Co/NF, the Te-Co/NF catalyst prepared with low concentration of Na₂TeO₃ is metallic Co phase. With the increase of Na₂TeO₃ concentration, the phase gradually changes into a mixed phase of metallic Co and CoTe. When the Na₂TeO₃ concentration is 30 mM, the prepared catalyst is pure CoTe, and the phase is pure Te while the concentration is 50 mM (Fig. S20). Different from Se-Co/NF and Te-Co/NF, the phase of S-Co/NF always remains metallic Co as the concentration of SC(NH₂)₂ increases (Fig. S21).

In addition, the effects of CS(NH₂)₂, SeO₂ and Na₂TeO₃ concentrations on the loading, morphology and non-metal content of different catalysts were investigated. The loading of different catalysts is shown in Table S7. The change of concentration has no significant effect on the loading of catalysts. The morphology of S-Co/NF catalysts does not change with the increase of CS(NH₂)₂ concentration (Fig. S22), while

the particle size of the Se-Co/NF and Te-Co/NF catalysts is decreased with the increase of SeO₂ and Na₂TeO₃ concentration (Fig. S23 and S24). Moreover, the contents of S, Se and Te in the catalysts are increased with the increase of CS(NH₂)₂, SeO₂ and Na₂TeO₃ concentrations (Table S8-S10). Combining the electrocatalytic performance of different catalysts, it can be found that moderate S and Te content in S-Co/NF and Te-Co/NF is conducive to the improvement of catalytic performance, while high Se content is beneficial for improving the performance of Se-Co/NF.

To explore the effect of unsaturated coordination Co–M bonds on the catalytic performance of metallic Co, the HER activities of Co/NF and the optimized M-Co/NF were analyzed. According to the LSV curves, the overpotentials at 10 mA cm⁻² and Tafel slopes of M-Co/NF surpass the pure Co/NF, suggesting the formation of Co–M bonds can enhance the HER performance and reaction kinetics of M-Co/NF (Fig. 3a-c). Considering the difference of M-Co/NF catalysts on morphology and M content, the intrinsic activities are evaluated by TOF. The TOF values of P-Co/NF, S-Co/NF, Se-Co/NF and Te-Co/NF at 0.10 V are 3.03, 1.65, 0.56 and 0.75 s⁻¹, which is much higher than that of pure Co/NF (0.09 s⁻¹), confirming that the formation of unsaturated coordination Co–M bonds greatly enhances the intrinsic catalytic activity of M-Co/NF (Fig. 3d). More importantly, compared to the S-Co/NF, Se-Co/NF and Te-Co/NF, the P-Co/NF possesses the lowest overpotential and Tafel slope, as well as highest TOF value at 0.10 V, indicate that P-Co/NF exhibits superior performance.

To explore the effect of unsaturated coordination Co–P bonds on HER performance of the P-Co catalyst, the Co₂P/NF, Co/NF and Pt/C/NF were also tested at the same condition. Fig. 4a displays the linear sweep voltammetry (LSV) curves. The P-Co/NF catalyst demonstrates superior HER performance with ultralow overpotentials of 23 and 85 mV at 10 and 100 mA cm⁻² (Fig. 4c), respectively, significantly lower than Co₂P/NF (88 mV@10 mA cm⁻² and 165 mV@100 mA cm⁻²) and Co/NF (176 mV@10 mA cm⁻² and 306 mV@100 mA cm⁻²), even better than Pt/C/NF (27 mV@10 mA cm⁻² and 138 mV@100 mA cm⁻²). The Tafel slope can

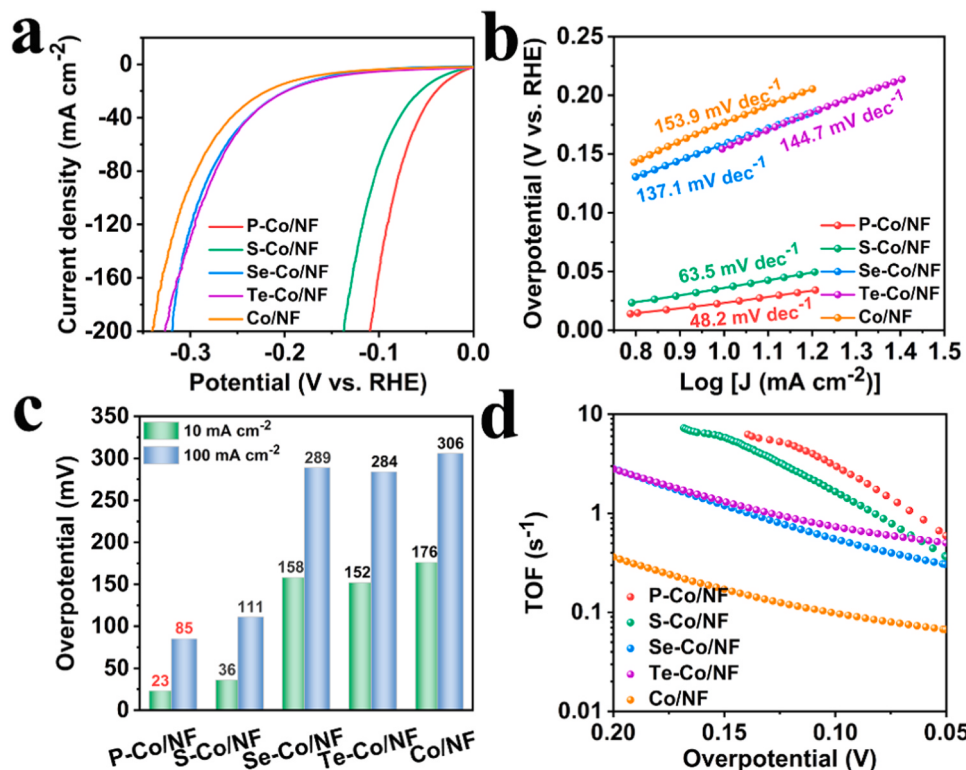


Fig. 3. (a) LSV curves, (b) Tafel plots, (c) comparison of overpotentials, (d) TOF values of P-Co/NF, S-Co/NF, Se-Co/NF, Te-Co/NF and Co/NF.

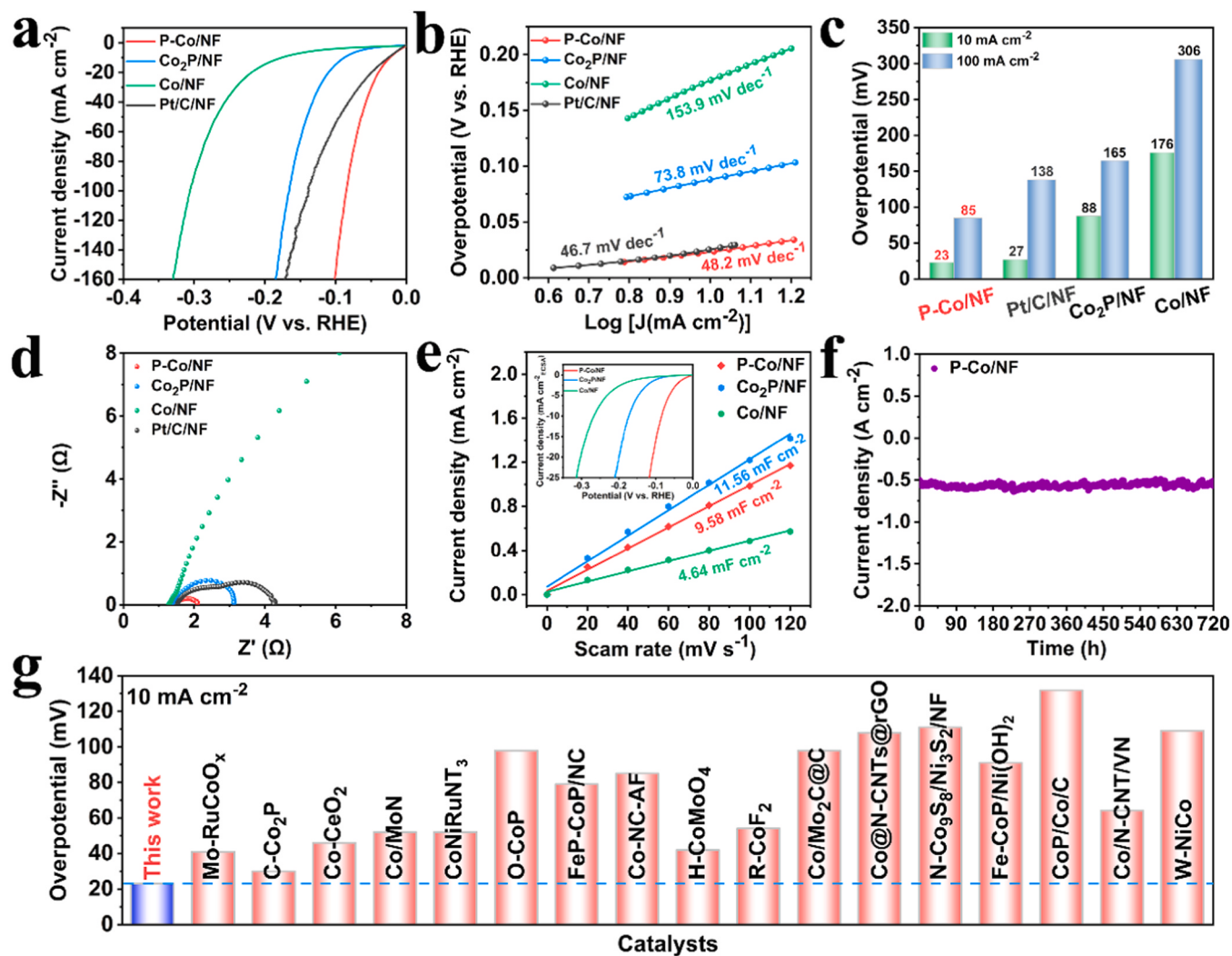


Fig. 4. (a) HER polarization curves and (b) corresponding Tafel plots of different catalysts, (c) comparison of overpotentials for all catalysts, (d) EIS curves and (e) C_{dl} and the HER polarization curves normalized by ECSA of different catalysts, (f) i-t curves of P-Co/NF at -0.890 V, (g) comparison of overpotentials of P-Co/NF with recently reported Co based HER catalysts.

reveal the reaction mechanism and kinetics and the Tafel analysis should acquire the data in a steady state [47]. Considering that the low overpotential region can be regarded as a steady state, the Tafel slopes were analyzed at the region of near 10 mA cm⁻². P-Co/NF possesses a Tafel slope value of 48.2 mV dec⁻¹ (Fig. 4b), less than that of Co₂P/NF (73.8 mV dec⁻¹),

Co/NF (153.9 mV dec⁻¹) and close to Pt/C/NF (46.7 mV dec⁻¹), implying that the formation of unsaturated Co–P bond significantly enhances the HER kinetics [10]. In addition, the current density of P-Co/NF is close to that of Pt/C/NF at low overpotential, while at high overpotential, the current density of P-Co/NF is notably larger. The current density is related to the reaction kinetics, diffusion, and the coverage of the reactants and intermediates (that is the number of active sites). The larger current density of P-Co/NF at high overpotential may be due to its low impedance, high number of active sites and good diffusion. Moreover, electrochemical impedance spectroscopy (EIS) was adopted to analyze the interfacial charge transfer kinetics. According to the EIS curves and the fitting results (Fig. 4d and S25), the charge transfer resistance (R_{ct}) of P-Co/NF is 0.56 Ω, which is smaller than that of Co₂P/NF (1.84 Ω), Co/NF (27.38 Ω) and Pt/C/NF (1.65 Ω), representing the fast interfacial charge transfer rate of P-Co/NF (Table S11).

To reveal the effect of the unsaturated Co–P bonds on intrinsic activity, the electrochemical active surface area (ECSA) was evaluated by

double layer capacitance (C_{dl}). The C_{dl} of P-Co/NF is 9.58 mF cm⁻², which is smaller than the Co₂P/NF (11.56 mF cm⁻²) but superior to Co/NF (4.64 mF cm⁻²), implying that the overall number of active sites for P-Co/NF has been increased (Figs. S26 and 4e). The normalized LSV curves of all catalysts by ECSA display that the P-Co/NF owns the lowest potential at normalized 10 mA cm⁻²EC_{SA}, suggesting the Co–P bonds greatly improve the intrinsic activity (Fig. 4e). Similarly, mass normalized LSV curves further verify the better intrinsic activity of P-Co/NF (Fig. S27). Moreover, the P-Co/NF exhibits the highest turnover frequency (TOF) of 3.03 s⁻¹ at 100 mV, further indicating that the formation of unsaturated coordination Co–P bonds significantly improves the inherent catalytic activity (Fig. S28). The multi-current process of P-Co/NF was tested to analyze the catalytic stability. When applying a current density of 20 mA cm⁻², the potential quickly stabilizes at -0.09 V (vs. RHE) and remains stable, similar phenomena also display at other current densities, confirming that P-Co/NF has excellent robustness and mass transfer capacity (Fig. S29)[48,49]. In addition, the durability of different catalysts was evaluated, and Pt/C/NF, Co/NF and Co₂P/NF all exhibit serious decline after 50 h test. However, the attenuation of P-Co/NF can be negligible at 20 mA cm⁻² (Fig. S30). The stability of the P-Co/NF has also been tested at 100 mA cm⁻² and the current density remains 93.1% after 50 h i-t test (Fig. S31). More importantly, even at a large current density of 0.5 A cm⁻², the P-Co/NF

can still run stably for 720 h, confirming its superior durability (Fig. 4f). Surprisingly, the high HER performance of P-Co/NF is better than most reported Co-based catalysts (Fig. 4g and Table S12). Moreover, the XRD, SEM and TEM images of P-Co after HER durability are consistent well with the primal condition, indicating that the high HER durability is induced by the super structure robustness (Fig. S32-S34). To evaluate the Faraday efficiency of P-Co/NF, the volume of H₂ was recorded by microgas flowmeter at 10 mA cm⁻². As shown in Fig. S35, compared with the theoretical value of H₂ generation, the Faraday efficiency of P-Co/NF is 98.1 %. To further explore the role of Co and P in HER, 10 mM thiocyanate ion (SCN⁻) and dodecanethiol were added into 1.0 M KOH to poison the Co sites and P sites, respectively. As shown in Fig. S36, when poisoning Co sites and P sites, the overpotentials of P-Co/NF at 10 mA cm⁻² increase from the initial 23 mV to 79 mV and 102 mV, respectively. After poisoning the P sites, the performance damps more obviously, indicating that the P sites play a major role in HER. Nevertheless, the excellent activity of P-Co/NF is inseparable from the synergistic effect of Co and P.

To elucidate the excellent activities of P-Co/NF, the XPS spectra after HER durability at 20 mA cm⁻² were tested. The binding energy of Co⁰ and P 2p_{3/2} negatively shift 0.17 and 0.16 eV, respectively, compared with the initial state (Fig. S37), manifesting that the Co and P atoms are reduced to a lower valence state during HER process. In addition, the proportion of Co⁰ is decreased and P–O substances are increased after the HER durability test, which is attributed to the reduction of Co atoms on the catalyst surface to highly active metal Co and subsequent natural oxidation [28].

Based on the above results, it is found that the P-Co/NF possesses better HER activity than the compound Co₂P/NF. To compare the performance between S-Co/NF, Se-Co/NF, and Te-Co/N catalysts and their compounds, the compounds of Co₉S₈, Co_{0.85}Se and CoTe were prepared (Fig. S38 and Table S13). Among them, Co₉S₈/NF displays an interlaced nanosheet morphology, while Co_{0.85}Se/NF and CoTe/NF are composed of stacked nanoparticles (Fig. S39). Moreover, the Co₉S₈/NF and CoTe/NF display a larger overpotential of 190 and 341 mV at 10 mA cm⁻² with sluggish reaction kinetics compared with S-Co/NF (36 mV) and Te-

Co/NF (152 mV). While the Co_{0.85}Se/NF shows a low overpotential of 100 mV at 10 mA cm⁻² with reduced Tafel slope compared with Se-Co/NF (158 mV) (Fig. S40). The higher catalytic activity of Co_{0.85}Se/NF may be related to its higher Se content, which is consistent with the results of changing the Se content. The stability of S-Co/NF, Se-Co/NF, Te-Co/NF and their compounds is shown in Fig. S41. S-Co/NF, Se-Co/NF and Te-Co/NF display better durability at 20 mA cm⁻² for 50 h than the Co₉S₈/NF, Co_{0.85}Se/NF and CoTe/NF. The increased current density of S-Co/NF and Se-Co/NF may be related to the reduction of the catalyst to the highly active low valence of Co under the reduction potential.

3.3. Electrocatalytic mechanism of M-Co/NF

DFT calculation was carried out to further explore the HER reaction mechanism. According to the experiment results, the Co (001) plane was adopted to simulate the pure Co. Considering the irregular distribution of P atoms on the P-Co surface, two P atoms adsorbed on Co (001) serve as the P-Co model. Fig. S42a shows the possible position of P atoms on Co (001). After structural optimization, the total system energy of different models was obtained and the model 5 has the lowest energy, indicating that the model 5 has the most stable structure (Fig. S42b). The differential charge density is first used to clarify the influence of Co–P bond on the local charge distribution of P-Co. As shown in Fig. 5a and b, the region around the P atom displays electron accumulation, while the Co atoms bonded with P atom and the Co–P bonding region demonstrate electron depletion, indicating that electrons are transferred from Co atoms to P atoms through Co–P bond. Fig. 5c shows the charge density distribution of P-Co. It can be clearly observed that the electron density around the P atom is relatively high, which further confirms the electrons transfer process. Due to part of the electrons transfer from Co to P atoms, the electrons that can transfer from Co site to H^{*} intermediate are reduced, thus weakening the adsorption of H^{*} at the Co sites [24].

Additionally, the adsorption energy (ΔE) of H₂O molecule on Co and P-Co was calculated. The ΔE of H₂O molecule on P-Co is -0.62 eV and

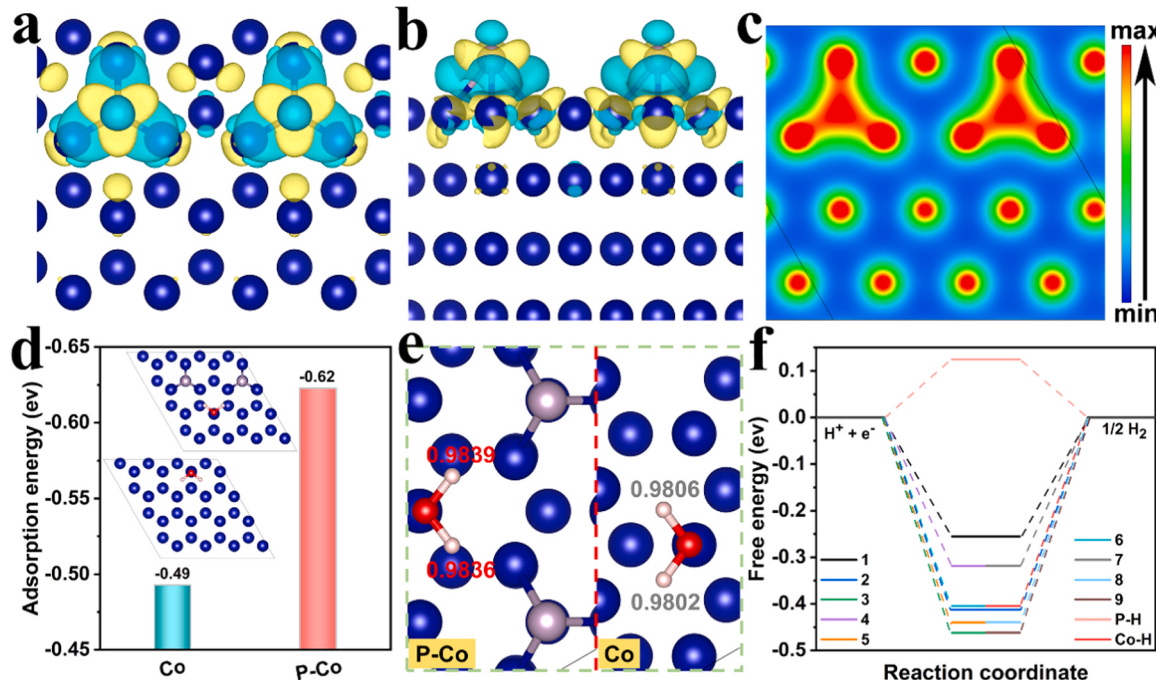


Fig. 5. (a, b) Differential charge density of P-Co (Yellow isosurfaces, electron accumulation; cyan isosurfaces, electron depletion.), (c) the charge density contour plot of the P-Co. (d) adsorption energy of H₂O on Co and P-Co. (e) the length of O–H bond in the optimized H₂O adsorption model of P-Co and Co. (f) ΔG_{H^*} on different sites of Co and P-Co. Color code: blue, Co; gray, P; red, O; white, H.

significantly stronger than pure Co (-0.49 eV), demonstrating that the formation of unsaturated coordination Co–P bonds enhances the adsorption of P-Co for H_2O molecules (Fig. 5d). Moreover, in the optimized H_2O adsorption model, the Co–O bond length in P-Co is 2.197 \AA , which is shorter than that of pure Co (2.222 \AA), confirming the stronger interaction between H_2O and Co atoms in P-Co (Fig. S43).

Through further analysis of the optimized H_2O adsorption model, the O–H bonds in H_2O molecules adsorbed on P-Co point to P atoms, and the bond lengths of O–H are 0.9839 and 0.9836 \AA , respectively, slightly longer than that of H_2O molecules adsorbed on pure Co (0.9806 and 0.9802 \AA), indicating that P atoms can pull the O–H bonds by attracting H atoms of H_2O molecules, thus promoting the dissociation process of H_2O molecules (Fig. 5e)[50]. In the previous study, the H intermediates are preferentially adsorbed on metal hollow sites[28,29,51], so the adsorption free energy of H intermediates (ΔG_{H^*}) at Co hollow site of pure Co and different sites of P-Co were calculated (Fig. S44). As shown in Figs. S44c and 5f, the ΔG_{H^*} of the hollow site for pure Co is -0.405 eV. After screening the possible active sites of P-Co, the hollow site 1 located between two P atoms exhibits a more thermally neutral ΔG_{H^*} (-0.255 eV), suggesting that the formation of unsaturated coordination Co–P bond significantly weakens the adsorption capacity of the Co site to H intermediate. In addition, the ΔG_{H^*} values of hollow sites 4 and 7 are both -0.318 eV, indicating that the Co–P bond optimizes the adsorption free energy of nearby Co sites, thereby transforming the inactive Co site into a highly active site. Moreover, the ΔG_{H^*} of P site is 0.124 eV, which is closer to 0 eV, implying that the P site also can act as the H adsorption site. Based on the above results, the formation of unsaturated coordination Co–P bonds facilitates the adsorption and dissociation of H_2O molecules, and optimizes the H adsorption capacity on Co sites and introduces a new P active site, therefore forming a situation where multiple active sites co-catalyzed HER process, which significantly enhances the HER catalytic activity of P-Co.

Based on the results of SEM-EDS, the atomic contents of S, Se and Te in different M-Co/NF catalysts are 7.6% , 6.0% and 8.0% , respectively, which is about half of the P contents (Table S14). Therefore, a M atom adsorbed on Co (001) hollow site was adopted to simulate the local active area of M-Co. According to the differential charge density of S-Co, Se-Co and Te-Co, cyan isosurface with electron depletion appears near the Co atom, while yellow isosurface with electron accumulation appears around the S, Se and Te atom, suggesting that electrons are transferred from Co atom to S/Se/Te atom through Co–S/Se/Te bonds

(Fig. 6a–c). In addition, ΔE of the H_2O molecule and ΔG_{H^*} of H intermediate on S-Co, Se-Co and Te-Co were calculated (Fig. S45). The ΔE of H_2O on S-Co, Se-Co and Te-Co is -0.572 , -0.573 and -0.559 eV, which is stronger than that of pure Co (-0.493 eV) (Fig. 6d). Moreover, the ΔG_{H^*} of S-Co, Se-Co and Te-Co is -0.284 , -0.282 and -0.285 eV, which is weaker than that of pure Co (-0.405 eV) (Fig. 6e). These results suggest that the introduction of S, Se and Te optimizes the adsorption of H_2O and H on metallic Co, thus enhancing the catalytic activity and reaction kinetics, which is consistent with the experimental results (Fig. 3). It is worth mentioning that the ΔE of H_2O molecule and ΔG_{H^*} of H intermediate on S-Co, Se-Co and Te-Co are all very close, but their HER performance differs greatly, which is related to the differences in morphology, nonmetallic atomic content, and loading on NF. Combined with the above results, the unsaturated coordination Co–M bonds regulates the local electronic structure of Co atoms nearby the Co–M bonds, thus enhancing the adsorption capacity of M-Co for H_2O and weakening the adsorption capacity for H, eventually improving the intrinsic activity of M-Co catalysts.

4. Conclusion

In summary, we adopted a facile and scalable electrodeposition strategy to synthesize a series of unsaturated coordination Co–M bonds modified metallic M-Co/NF (M = P, S, Se, Te) as high-efficiency alkaline HER catalysts. The incorporated non-metallic atoms not only regulate the local coordination environment of M-Co/NF, but also form the Co–M charge transport channel to facilitate charge redistribution. The precise local bonding structure optimizes the adsorption and activation of H_2O and the adsorption free energy of H intermediates, thus enhancing the inherent HER activities of M-Co/NF. More importantly, the optimized P-Co/NF possesses excellent HER performance which needs an ultralow overpotential of 23 and 85 mV to achieve 10 and 100 mA cm^{-2} with superior stability at large current density (0.5 A cm^{-2}). This work reports a general strategy to prepare surface unsaturated non-metallic chemical bonds modified metallic Co catalysts, and provides novel insight into the effects of the local coordination environment on activity and the rational design of efficient non-noble transition metal catalysts.

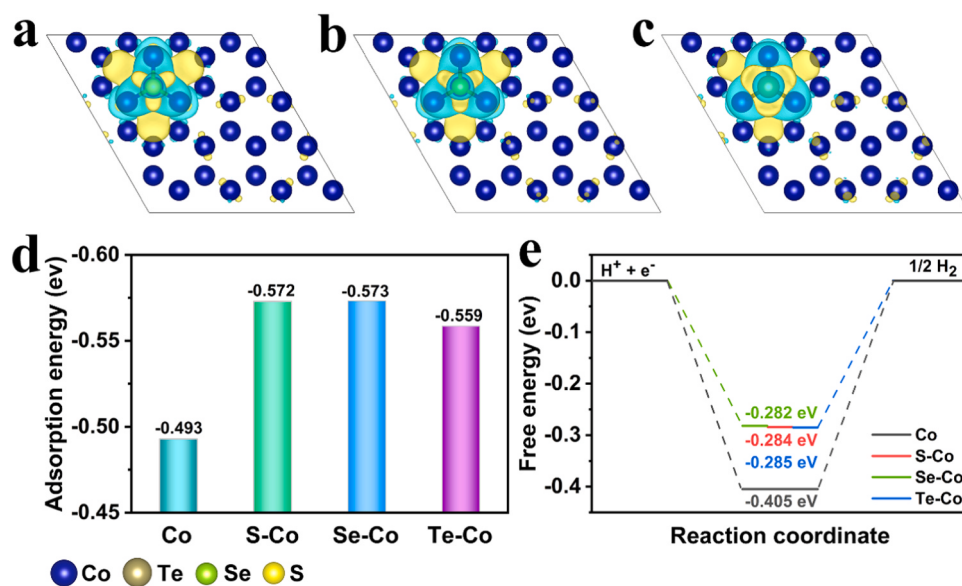


Fig. 6. Differential charge density of (a) S-Co, (b) Se-Co and (c) Te-Co, (d) ΔE of H_2O , (e) ΔG_{H^*} for Co, S-Co, Se-Co and Te-Co, respectively. Yellow and cyan isosurfaces represent electron accumulation and electron depletion, respectively.

CRediT authorship contribution statement

Hui Liu: Writing – review & editing, Conceptualization. **Xinghua Zhang:** Writing – review & editing, Project administration, Conceptualization. **Zunming Lu:** Investigation. **Zehao Zang:** Writing – original draft, Data curation, Conceptualization. **Chunyan Fan:** Software, Investigation. **Yangyang Ren:** Software, Investigation, Formal analysis. **Xiaojing Yang:** Visualization, Validation. **Xiaofei Yu:** Visualization, Validation. **Lanlan Li:** Validation, Methodology. **Yahui Cheng:** Supervision, Methodology.

Declaration of Competing Interest

The authors declare that they have no known competing financial interests or personal relationships that could have appeared to influence the work reported in this paper.

Data availability

Data will be made available on request.

Acknowledgements

This work was supported by the National Natural Science Foundation of China (No. 52271210, 22179032, 52171176), Natural Science Foundation of Hebei Province (No. E2021202022, B2021202011).

Appendix A. Supporting information

Supplementary data associated with this article can be found in the online version at [doi:10.1016/j.apcatb.2024.123912](https://doi.org/10.1016/j.apcatb.2024.123912).

References

- [1] X. Zhang, A. Wu, D. Wang, Y. Jiao, H. Yan, C. Jin, Y. Xie, C. Tian, Fine-tune the electronic structure in Co-Mo based catalysts to give easily coupled HER and OER catalysts for effective water splitting, *Appl. Catal. B* 328 (2023) 122474, <https://doi.org/10.1016/j.apcatb.2023.122474>.
- [2] X.L. Zhang, P.C. Yu, X.Z. Su, S.J. Hu, L. Shi, Y.H. Wang, P.P. Yang, F.Y. Gao, Z. Wu, L.P. Chi, Y.R. Zheng, M.R. Gao, Efficient acidic hydrogen evolution in proton exchange membrane electrolyzers over a sulfur-doped marcasite-type electrocatalyst, *Sci. Adv.* 9 (2023) eadh2885, <https://doi.org/10.1126/sciadv.adh2885>.
- [3] B. Wang, X. Chen, Y. He, Q. Liu, X. Zhang, Z. Luo, J.V. Kennedy, J. Li, D. Qian, J. Liu, G.I.N. Waterhouse, Fe₂O₃/P-doped CoMoO₄ electrocatalyst delivers efficient overall water splitting in alkaline media, *Appl. Catal. B* 346 (2024) 123741, <https://doi.org/10.1016/j.apcatb.2024.123741>.
- [4] R. Zhang, Y. Li, X. Zhou, A. Yu, Q. Huang, T. Xu, L. Zhu, P. Peng, S. Song, L. Echegoyen, F.F. Li, Single-atomic platinum on fullerene C(60) surfaces for accelerated alkaline hydrogen evolution, *Nat. Commun.* 14 (2023) 2460, <https://doi.org/10.1038/s41467-023-38126-z>.
- [5] B. Zhang, F. Yang, X. Liu, N. Wu, S. Che, Y. Li, Phosphorus doped nickel-molybdenum aerogel for efficient overall water splitting, *Appl. Catal. B* 298 (2021) 120494, <https://doi.org/10.1016/j.apcatb.2021.120494>.
- [6] Z. Li, J.Y. Fu, Y. Feng, C.K. Dong, H. Liu, X.W. Du, A silver catalyst activated by stacking faults for the hydrogen evolution reaction, *Nat. Catal.* 2 (2019) 1107–1114, <https://doi.org/10.1038/s41929-019-0365-9>.
- [7] Y. Pan, J. Gao, E. Lv, T. Li, H. Xu, L. Sun, A. Nairan, Q. Zhang, Integration of alloy segregation and surface Co–O hybridization in carbon-encapsulated CoNiPt alloy catalyst for superior alkaline hydrogen evolution, *Adv. Funct. Mater.* 33 (2023) 2303833, <https://doi.org/10.1002/adfm.202303833>.
- [8] J. Greeley, T.F. Jaramillo, J. Bonde, I.B. Chorkendorff, J.K. Nørskov, Computational high-throughput screening of electrocatalytic materials for hydrogen evolution, *Nat. Mater.* 5 (2006) 909–913, <https://doi.org/10.1038/nmat1752>.
- [9] J.K. Nørskov, T. Bligaard, A. Logadottir, J. Kitchin, J.G. Chen, S. Pandelov, U. Stimming, Trends in the exchange current for hydrogen evolution, *J. Electrochem. Soc.* 152 (2005), <https://doi.org/10.1149/1.1856988>. J23–J26.
- [10] J. Zhu, L. Hu, P. Zhao, L.Y.S. Lee, K.Y. Wong, Recent advances in electrocatalytic hydrogen evolution using nanoparticles, *Chem. Rev.* 120 (2020) 851–918, <https://doi.org/10.1021/acs.chemrev.9b00248>.
- [11] L. Deng, F. Hu, M. Ma, S.C. Huang, Y. Xiong, H.Y. Chen, L. Li, S. Peng, Electronic modulation caused by interfacial Ni-O/M (M=Ru, Ir, Pd) bonding for accelerating hydrogen evolution kinetics, *Angew. Chem. Int. Ed.* 60 (2021) 22276–22282, <https://doi.org/10.1002/anie.202110374>.
- [12] J. Mahmood, F. Li, S.M. Jung, M.S. Okyay, I. Ahmad, S.J. Kim, N. Park, H.Y. Jeong, J.B. Baek, An efficient and pH-universal ruthenium-based catalyst for the hydrogen evolution reaction, *Nat. Nanotechnol.* 12 (2017) 441–446, <https://doi.org/10.1038/nano.2016.304>.
- [13] M. Wang, Z. Wan, X. Meng, Z. Li, X. Ding, P. Li, C. Li, J.G. Wang, Z. Li, Heterostructured Co/Mo-sulfide catalyst enables unbiased solar water splitting by integration with perovskite solar cells, *Appl. Catal. B* 309 (2022) 121272, <https://doi.org/10.1016/j.apcatb.2022.121272>.
- [14] J.X. Liu, H.Y. Su, D.P. Sun, B.Y. Zhang, W.X. Li, Crystallographic dependence of CO activation on cobalt catalysts: HCP versus FCC, *J. Am. Chem. Soc.* 135 (2013) 16284–16287, <https://doi.org/10.1021/ja408521w>.
- [15] Y. Li, X. Tan, W. Yang, X. Bo, Z. Su, T. Zhao, S.C. Smith, C. Zhao, Vanadium oxide clusters decorated metallic cobalt catalyst for active alkaline hydrogen evolution, *Cell Rep. Phys. Sci.* 1 (2020) 100275, <https://doi.org/10.1016/j.xcrp.2020.100275>.
- [16] M. Cao, K. Liu, Y. Song, C. Ma, Y. Lin, H. Li, K. Chen, J. Fu, H. Li, J. Luo, Y. Zhang, X. Zheng, J. Hu, M. Liu, Regulating local charges of atomically dispersed Mo⁸⁺ sites by nitrogen coordination on cobalt nanosheets to trigger water dissociation for boosted hydrogen evolution in alkaline media, *J. Energy Chem.* 72 (2022) 125–132, <https://doi.org/10.1016/j.jechem.2022.04.046>.
- [17] Z. Chen, W. Gong, J. Wang, S. Hou, G. Yang, C. Zhu, X. Fan, Y. Li, R. Gao, Y. Cui, Metallic W/WO₂ solid-acid catalyst boosts hydrogen evolution reaction in alkaline electrolyte, *Nat. Commun.* 14 (2023) 5363, <https://doi.org/10.1038/s41467-023-41097-w>.
- [18] Y. Hao, D. Yu, S. Zhu, C.H. Kuo, Y.M. Chang, L. Wang, H.Y. Chen, M. Shao, S. Peng, Methanol upgrading coupled with hydrogen product at large current density promoted by strong interfacial interactions, *Energy Environ. Sci.* 16 (2023) 1100–1110, <https://doi.org/10.1039/D2EE03936B>.
- [19] J. Joo, T. Kim, J. Lee, S.I. Choi, K. Lee, Morphology-controlled metal sulfides and phosphides for electrochemical water splitting, *Adv. Mater.* 31 (2019) 1806682, <https://doi.org/10.1002/adma.201806682>.
- [20] H. Sun, X. Xu, Y. Song, W. Zhou, Z. Shao, Designing high-valence metal sites for electrochemical water splitting, *Adv. Funct. Mater.* 31 (2021) 2009779, <https://doi.org/10.1002/adfm.202009779>.
- [21] H. Wang, T. Zhai, Y. Wu, T. Zhou, B. Zhou, C. Shang, Z. Guo, High-valence oxides for high performance oxygen evolution electrocatalysis, *Adv. Sci.* 10 (2023) 2301706, <https://doi.org/10.1002/advs.202301706>.
- [22] Y. Zeng, M. Zhao, Z. Huang, W. Zhu, J. Zheng, Q. Jiang, Z. Wang, H. Liang, Surface reconstruction of water splitting electrocatalysts, *Adv. Energy Mater.* 12 (2022) 2201713, <https://doi.org/10.1002/aenm.202201713>.
- [23] Y. Wu, Y. Li, M. Yuan, H. Hao, X. San, Z. Lv, L. Xu, B. Wei, Operando capturing of surface self-reconstruction of Ni₃S₂/FeNi₂S₄ hybrid nanosheet array for overall water splitting, *Chem. Eng. J.* 427 (2022) 131944, <https://doi.org/10.1016/j.cej.2021.131944>.
- [24] J. Huang, J. Han, T. Wu, K. Feng, T. Yao, X. Wang, S. Liu, J. Zhong, Z. Zhang, Y. Zhang, B. Song, Boosting hydrogen transfer during volmer reaction at oxides/metal nanocomposites for efficient alkaline hydrogen evolution, *ACS Energy Lett.* 4 (2019) 3002–3010, <https://doi.org/10.1021/acsenergylett.9b02359>.
- [25] H. Jin, X. Wang, C. Tang, A. Vasileff, L. Li, A. Slattery, S.Z. Qiao, Stable and highly efficient hydrogen evolution from seawater enabled by an unsaturated nickel surface nitride, *Adv. Mater.* 33 (2021) 2007508, <https://doi.org/10.1002/adma.202007508>.
- [26] H. Jin, L. Li, X. Liu, C. Tang, W. Xu, S. Chen, L. Song, Y. Zheng, S.Z. Qiao, Nitrogen vacancies on 2D layered W₂N₃: A stable and efficient active site for nitrogen reduction reaction, *Adv. Mater.* 31 (2019) e1902709, <https://doi.org/10.1002/adma.201902709>.
- [27] S. Li, Y. Liu, K. Feng, C. Li, J. Xu, C. Lu, H. Lin, Y. Feng, D. Ma, J. Zhong, High valence state sites as favorable reductive centers for high-current-density water splitting, *Angew. Chem. Int. Ed.* 62 (2023) e202308670, <https://doi.org/10.1002/anie.202308670>.
- [28] Z. Zang, Q. Guo, X. Li, Y. Cheng, L. Li, X. Yu, Z. Lu, X. Yang, X. Zhang, H. Liu, Construction of a S and Fe co-regulated metal Ni electrocatalyst for efficient alkaline overall water splitting, *J. Mater. Chem. A* 11 (2023) 4661–4671, <https://doi.org/10.1039/D2TA09802D>.
- [29] J. Wang, S. Mao, Z. Liu, Z. Wei, H. Wang, Y. Chen, Y. Wang, Dominating role of Ni (0) on the interface of Ni/NiO for enhanced hydrogen evolution reaction, *ACS Appl. Mater. Interfaces* 9 (2017) 7139–7147, <https://doi.org/10.1021/acsmami.6b15377>.
- [30] F.Y. Yu, Z.L. Lang, L.Y. Yin, K. Feng, Y.J. Xia, H.-Q. Tan, H.T. Zhu, J. Zhong, Z. H. Kang, Y.G. Li, Pt–O bond as an active site superior to Pt⁰ in hydrogen evolution reaction, *Nat. Commun.* 11 (2020) 490, <https://doi.org/10.1038/s41467-019-14274-z>.
- [31] H. Jin, X. Liu, S. Chen, A. Vasileff, L. Li, Y. Jiao, L. Song, Y. Zheng, S.Z. Qiao, Heteroatom-doped transition metal electrocatalysts for hydrogen evolution reaction, *ACS Energy Lett.* 4 (2019) 805–810, <https://doi.org/10.1021/acsenergylett.9b00348>.
- [32] Y. Li, X. Tan, S. Chen, X. Bo, H. Ren, S.C. Smith, C. Zhao, Processable surface modification of nickel-heteroatom (N, S) bridge sites for promoted alkaline hydrogen evolution, *Angew. Chem. Int. Ed.* 58 (2019) 461–466, <https://doi.org/10.1002/anie.201808629>.
- [33] B. You, X. Liu, G. Hu, S. Gul, J. Yano, D.E. Jiang, Y. Sun, Universal surface engineering of transition metals for superior electrocatalytic hydrogen evolution in neutral water, *J. Am. Chem. Soc.* 139 (2017) 12283–12290, <https://doi.org/10.1021/jacs.7b06434>.

[34] J. Wang, L. Zhu, G. Dharan, G.W. Ho, Electrodeposited cobalt phosphide superstructures for solar-driven thermoelectrocatalytic overall water splitting, *J. Mater. Chem. A* 5 (2017) 16580–16584, <https://doi.org/10.1039/c7ta04719c>.

[35] J. Xu, G. Shao, X. Tang, F. Lv, H. Xiang, C. Jing, S. Liu, S. Dai, Y. Li, J. Luo, Z. Zhou, Frenkel-defected monolayer MoS₂ catalysts for efficient hydrogen evolution, *Nat. Commun.* 13 (2022) 2193, <https://doi.org/10.1038/s41467-022-29929-7>.

[36] S. Anantharaj, S. Noda, Amorphous catalysts and electrochemical water splitting: an untold story of harmony, *Small* 16 (2020) e1905779, <https://doi.org/10.1002/smll.201905779>.

[37] M. Li, X. Wang, K. Liu, Z. Zhu, H. Guo, M. Li, H. Du, D. Sun, H. Li, K. Huang, Y. Tang, G. Fu, Ce-induced differentiated regulation of Co sites via gradient orbital coupling for bifunctional water-splitting reactions, *Adv. Energy Mater.* 13 (2023) 2301162, <https://doi.org/10.1002/aenm.202301162>.

[38] X. Wang, J. Zhang, P. Wang, L. Li, H. Wang, D. Sun, Y. Li, Y. Tang, X.F. Lu, Y. Wang, G. Fu, Terbium-induced cobalt valence-band narrowing boosts electrocatalytic oxygen reduction, *Energy Environ. Sci.* 16 (2023) 5500–5512, <https://doi.org/10.1039/d3ee02503a>.

[39] M.R. Kandel, U.N. Pan, P.P. Dhakal, R.B. Ghising, T.T. Nguyen, J. Zhao, N.H. Kim, J.H. Lee, Unique heterointerface engineering of Ni₂P–MnP nanosheets coupled Co₂P nanoflowers as hierarchical dual-functional electrocatalyst for highly proficient overall water-splitting, *Appl. Catal. B* 331 (2023) 122680, <https://doi.org/10.1016/j.apcatb.2023.122680>.

[40] L. Yang, X. Cao, X. Wang, Q. Wang, L. Jiao, Regulative electronic redistribution of CoTe₂/CoP heterointerfaces for accelerating water splitting, *Appl. Catal. B* 329 (2023) 122551, <https://doi.org/10.1016/j.apcatb.2023.122551>.

[41] K. Dong, D.T. Tran, X. Li, S. Prabhakaran, D.H. Kim, N.H. Kim, J.H. Lee, Three-phase interface engineering via P-doped CoMo₂S₄-integrated Co₄S₃/Co₂P enables high-efficiency overall water splitting, *Appl. Catal. B* 344 (2024) 123649, <https://doi.org/10.1016/j.apcatb.2023.123649>.

[42] Y. Lin, K. Sun, X. Chen, C. Chen, Y. Pan, X. Li, J. Zhang, High-precision regulation synthesis of Fe-doped Co₂P nanorod bundles as efficient electrocatalysts for hydrogen evolution in all-pH range and seawater, *J. Energy Chem.* 55 (2021) 92–101, <https://doi.org/10.1016/j.jechem.2020.06.073>.

[43] W. Xu, G. Fan, S. Zhu, Y. Liang, Z. Cui, Z. Li, H. Jiang, S. Wu, F. Cheng, Electronic structure modulation of nanoporous cobalt phosphide by carbon doping for alkaline hydrogen evolution reaction, *Adv. Funct. Mater.* 31 (2021) 2107333, <https://doi.org/10.1002/adfm.202107333>.

[44] Q. Shao, Y. Wang, S. Yang, K. Lu, Y. Zhang, C. Tang, J. Song, Y. Feng, L. Xiong, Y. Peng, Y. Li, H.L. Xin, X. Huang, Stabilizing and activating metastable nickel nanocrystals for highly efficient hydrogen evolution electrocatalysis, *ACS Nano* 12 (2018) 11625–11631, <https://doi.org/10.1021/acsnano.8b06896>.

[45] X. Wu, F. Chen, N. Zhang, Y. Lei, Y. Jin, A. Qaseem, R.L. Johnston, Activity trends of binary silver alloy nanocatalysts for oxygen reduction reaction in alkaline media, *Small* 13 (2017) 1603387, <https://doi.org/10.1002/smll.201603387>.

[46] B. You, N. Jiang, M. Sheng, S. Gul, J. Yano, Y. Sun, High-performance overall water splitting electrocatalysts derived from cobalt-based metal–organic frameworks, *Chem. Mater.* 27 (2015) 7636–7642, <https://doi.org/10.1021/acs.chemmater.5b02877>.

[47] S. Anantharaj, S. Noda, M. Driess, P.W. Menezes, The pitfalls of using potentiodynamic polarization curves for tafel analysis in electrocatalytic water splitting, *ACS Energy Lett.* (2021) 1607–1611, <https://doi.org/10.1021/acsenergylett.1c00608>.

[48] Z. Zang, X. Wang, X. Li, Q. Zhao, L. Li, X. Yang, X. Yu, X. Zhang, Z. Lu, Co₉S₈ nanosheet coupled Cu₂S nanorod heterostructure as efficient catalyst for overall water splitting, *ACS Appl. Mater. Interfaces* 13 (2021) 9865–9874, <https://doi.org/10.1021/acsami.0c20820>.

[49] D. Wu, Y. Wei, X. Ren, X. Ji, Y. Liu, X. Guo, Z. Liu, A.M. Asiri, Q. Wei, X. Sun, Co (OH)₂ nanoparticle-encapsulating conductive nanowires array: room-temperature electrochemical preparation for high-performance water oxidation electrocatalysis, *Adv. Mater.* 30 (2018) 1705366, <https://doi.org/10.1002/adma.201705366>.

[50] Y. Liu, Q. Li, R. Si, G.D. Li, W. Li, D.P. Liu, D. Wang, L. Sun, Y. Zhang, X. Zou, Coupling sub-nanometric copper clusters with quasi-amorphous cobalt sulfide yields efficient and robust electrocatalysts for water splitting reaction, *Adv. Mater.* 29 (2017) 1606200, <https://doi.org/10.1002/adma.201606200>.

[51] J. Wang, S. Xin, Y. Xiao, Z. Zhang, Z. Li, W. Zhang, C. Li, R. Bao, J. Peng, J. Yi, S. Chou, Manipulating the water dissociation electrocatalytic sites of bimetallic Ni-based alloy for highly-efficient alkaline hydrogen evolution, *Angew. Chem. Int. Ed.* 61 (2022) e202202518, <https://doi.org/10.1002/anie.202202518>.